

Imaging mesoscale upper ocean dynamics using synthetic aperture radar and optical data

Vladimir Kudryavtsev,^{1,2,3} Alexander Myasoedov,^{1,2} Bertrand Chapron,⁴ Johnny A. Johannessen,^{5,6} and Fabrice Collard⁷

Received 11 August 2011; revised 17 January 2012; accepted 29 February 2012; published 19 April 2012.

[1] A synergetic approach for quantitative analysis of high-resolution ocean synthetic aperture radar (SAR) and imaging spectrometer data, including the infrared (IR) channels, is suggested. This approach first clearly demonstrates that sea surface roughness anomalies derived from Sun glitter imagery compare very well to SAR roughness anomalies. As further revealed using these fine-resolution (~ 1 km) observations, the derived roughness anomaly fields are spatially correlated with sharp gradients of the sea surface temperature (SST) field. To quantitatively interpret SAR and optical (in visible and IR ranges) images, equations are derived to relate the “surface roughness” signatures to the upper ocean flow characteristics. As developed, a direct link between surface observations and divergence of the sea surface current field is anticipated. From these satellite observations, intense cross-frontal dynamics and vertical motions are then found to occur near sharp horizontal gradients of the SST field. As a plausible mechanism, it is suggested that interactions of the wind-driven upper layer with the quasi-geostrophic current field (via Ekman advective and mixing mechanisms) result in the generation of secondary ageostrophic circulation, producing convergence and divergence of the surface currents. The proposed synergetic approach combining SST, Sun glitter brightness, and radar backscatter anomalies, possibly augmented by other satellite data (e.g., altimetry, scatterometry, ocean color), can thus provide consistent and quantitative determination of the location and intensity of the surface current convergence/divergence (upwelling/downwelling). This, in turn, establishes an important step toward advances in the quantitative interpretation of the upper ocean dynamics from their two-dimensional satellite surface expressions.

Citation: Kudryavtsev, V., A. Myasoedov, B. Chapron, J. A. Johannessen, and F. Collard (2012), Imaging mesoscale upper ocean dynamics using synthetic aperture radar and optical data, *J. Geophys. Res.*, 117, C04029, doi:10.1029/2011JC007492.

1. Introduction

[2] Satellite optical imagery provides regular observations of the ocean color and the sea surface temperature (SST) field, offering fascinating expressions of surface patterns at different scales from hundreds of kilometers down to about 1 km resolution. These observations often reveal the richness, complexity, and mesoscale to submesoscale heterogeneity of the upper ocean dynamics and the interaction with biological processes.

[3] Based on very different principles, imaging radars, better known as synthetic aperture radars (SARs), also often provide spectacular manifestations of mesoscale and submesoscale ocean surface signatures. In such cases, the image contrasts are associated with the ocean surface roughness variations linked to changes in the near-surface winds, waves, and currents, as well as the presence of surface contaminants. As a key aspect, current shears and ageostrophic motions have the potential to affect the short-scale surface wave energy very locally, resulting in enhanced or suppressed radar-detectable roughness changes [see, e.g., Marmorino *et al.*, 1994; Johannessen *et al.*, 1996; Jansen *et al.*, 1998; Kudryavtsev *et al.*, 2005; Johannessen *et al.*, 2005]. Practical forward radar imaging models of surface current features in the presence of varying surface wind forcing have been previously developed to advance the quantitative interpretation of the high-resolution radar observations [Alpers and Hennings, 1984; Romeiser and Alpers, 1997; Kudryavtsev *et al.*, 2005]. Though the ability of SAR to detect surface phenomena is restricted to “favorable” low to moderate wind speed conditions, the high spatial resolution, wide coverage, SAR imaging capabilities make it a

¹Nansen International Environmental and Remote Sensing Center, St. Petersburg, Russia.

²Also at Russian State Hydrometeorological University, St. Petersburg, Russia.

³Also at Marine Hydrophysical Institute, Sevastopol, Ukraine.

⁴Institute Français de Recherche pour l'Exploitation de la Mer, Plouzané, France.

⁵Nansen Environmental and Remote Sensing Center, Bergen, Norway.

⁶Also at Geophysical Institute, University of Bergen, Bergen, Norway.

⁷Direction of Radar Applications, CLS, Plouzané, France.

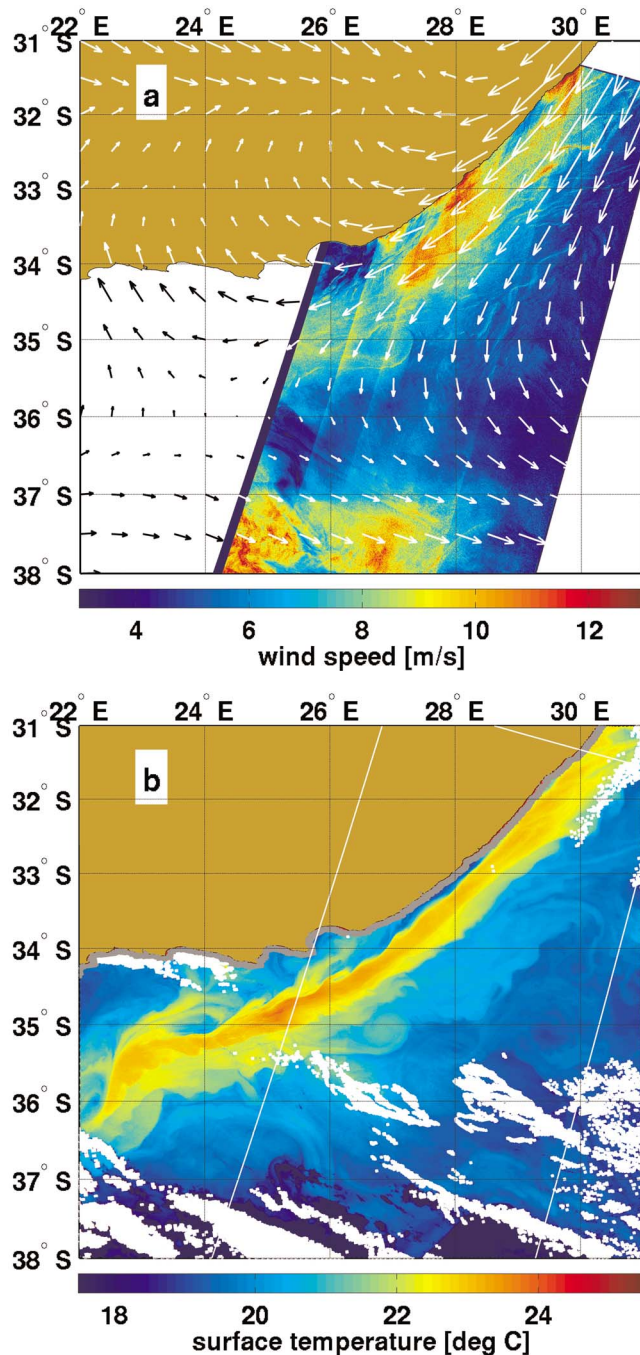


Figure 1. (a) Advanced synthetic aperture radar (ASAR) wind speed image (18 November 2007, 07:24 GMT) presented in terms of wind speed field derived using the CMOD4 algorithm with the direction (white arrows) taken from National Centers for Environmental Prediction (NCEP) model. (b) Sea surface temperature (SST) field derived from the Moderate Resolution Imaging Spectroradiometer (MODIS) image (18 November, 2007, 12:05 GMT). White areas are cloud masked.

powerful instrument to investigate various oceanic phenomena, e.g., internal waves, mesoscale surface current features including filaments, meandering fronts and eddies, as well as biogenic and oil slicks [e.g., Gasparovic et al., 1988;

Lyzenga and Bennett, 1988; Johannessen et al., 1996; Beal et al., 1997; Espedal et al., 1998; Gade et al., 1998].

[4] A more consistent use of high-resolution satellite imagery in the visible, infrared, and microwave bands can therefore strengthen the opportunity to advance toward an integrated analysis tool for better quantitative retrieval of the upper ocean dynamics. As illustrated in Figure 1, for instance, it is revealed that coincident images of SST patterns and sea surface SAR roughness features expressed in terms of wind speed contain expressions of sharp SST changes almost precisely collocated with elongated features of bright/dark SAR wind speed anomalies (see also Lin et al. [2002] as an example of synergetic analysis of SAR backscatter, ocean color (Chl *a*) and SST in the upwelling region).

[5] To gain confidence in such interpretations, our present objective is to further introduce the potential use of an often neglected quantitative contemporaneous source of information. Under favorable imaging geometry near the Sun glitter area, reflected sunlight radiations measured by satellite imaging spectrometers (e.g., by the Moderate Resolution Imaging Spectroradiometer (MODIS) or Medium Resolution Imaging Spectroradiometer (MERIS) instrument) represent the major part of the outgoing radiation. Sun glitter possesses valuable quantitative information on statistical properties of the short wind waves [Cox and Munk, 1954]. Spatial variations of these properties caused by variable wind, surface slicks, and surface currents can therefore become visible in the Sun glitter areas as measurable contrasts of the sea surface brightness signals [see, e.g., Munk et al., 2000; Jackson, 2007; Hennings et al., 1994; Hu et al., 2009]. Recently, a new method has been developed to exploit the Sun glitter signatures of ocean phenomena in terms of variations of the sea surface roughness mean squared slope (MSS) [Kudryavtsev et al., 2012]. Potentially, the MSS retrievals from optical sensors can thus be considered complementary to the SAR derived normalized radar cross section (NRCS) anomalies and be used to constrain the quantitative interpretations of mesoscale and submesoscale surface phenomena expressed in infrared, color, and radar backscatter satellite images.

[6] The main goal of the present study is thus to assess and demonstrate the high degree of correspondence between detected contrasts from satellite SAR and multispectral optical observations and to suggest an advanced approach for the investigation of surface manifestation of the mesoscale upper ocean dynamics. In section 2 we present the data followed by a discussion of the common physics behind the similarity in the Sun glitter MSS and SAR NRCS expressions of the mesoscale features. A quantitative retrieval of the surface current properties, based on the use of the SST image, is presented in section 3, followed by an analysis and discussion of the relation between the divergence of surface current fields and the observed NRCS and the MSS anomalies and the radar imaging model simulation results. The summary and conclusion are then presented in section 4.

2. SAR and Sun Glitter Signatures of the Surface Currents

2.1. Observations

[7] The study strongly capitalizes on the synergy of MODIS and SAR imagery of the Agulhas current area

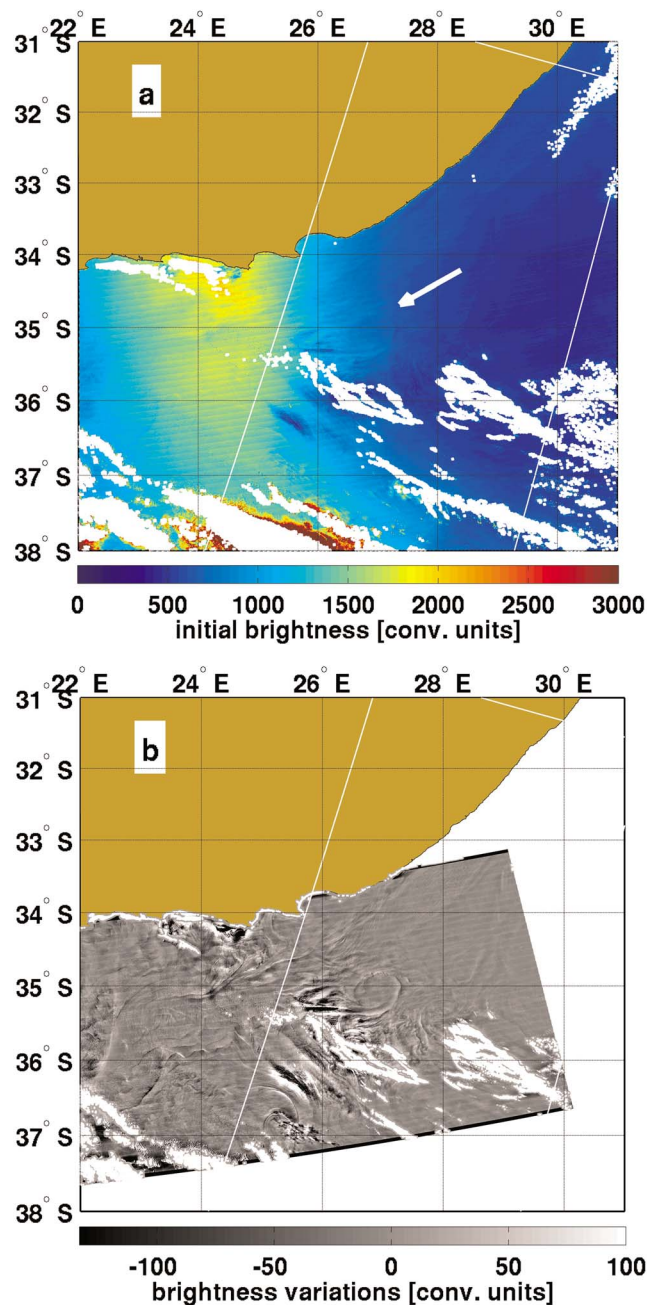


Figure 2. (a) Aqua MODIS image in the red channel with a 250 m resolution of the Agulhas Current area (acquired on 18 November 2007, 12:05) marking a distinct strip-like structure of the Sun glitter area which is typical for the MODIS Sun glitter imagery. White arrow indicates a brightness feature corresponding to the surface manifestation of the ocean current. (b) The corresponding Sun glitter brightness variations ($\tilde{B} = B - \bar{B}$) depicting a variety of “small-scale” surface features. Brightness of the image and its variations are given in conventional units. White areas are the clouds mask, and South Africa is marked in brown.

acquired 5 h apart on 18 November 2007. The greater Agulhas Current regime is highly dynamic and characterized by a wide range of mesoscale and submesoscale processes and features including meanders, fronts, filaments, and eddies. The region,

moreover, is also often favorable for Sun glitter analysis based on the MODIS data. Figure 1 displays the wind field derived from the Envisat advanced SAR (ASAR) wide-swath image acquired on 18 November 2007, 07:24 GMT, using the CMOD4 transfer function [Stoffelen and Anderson, 1997] with a prescribed wind field direction taken from the National Centers for Environmental Prediction (NCEP) model, and the SST field derived from the MODIS image (acquired less than 5 h apart on 12:05 GMT) using a standard retrieval algorithm. The wind speed varies from 4 m/s to 13 m/s, but a variety of distinct features presumably caused by the oceanic mesoscale variability, including meandering fronts and eddies, are also revealed, in particular bounded by 34°–35.5°N and 26°–30°E. These features are also clearly expressed in the SST field. Thus, both the SST and SAR fields apparently possess surface signatures of the same mesoscale upper ocean dynamic phenomena.

[8] The original Aqua MODIS image in the red channel (645 nm) at 250 m resolution is shown in Figure 2a and clearly reveals both the Sun glitter and the presence of clouds. The Sun glitter has a “strip-like structure” typical for the MODIS imagery. A surface brightness feature to the right of the Sun glitter (marked by the arrow) is also visible, that may be interpreted as surface manifestation of the ocean currents. By decomposing the original brightness on the smoothed brightness \bar{B} (averaging scale $30 \times 30 \text{ km}^2$) and its variations \tilde{B} , the remarkable details of the latter feature become more distinct as revealed by the presence of the 80 km in diameter anticyclonic (rotating anticlockwise) shaped eddy shown in Figure 2b. The full description of the method for the retrieval of such anomalies in the Sun glitter brightness variations associated with changes in the mean square slope of the sea surface is given by Kudryavtsev *et al.* [2012].

[9] The sea surface mean square slope (MSS) contrasts derived from these Sun glitter brightness variations are defined as $K_s = (s^2 - \bar{s}_0^2) / \bar{s}_0^2$, where \bar{s}_0^2 is the MSS averaged over the $30 \text{ km} \times 30 \text{ km}$ window. The pattern of the MSS contrasts (see Figure 3a) is even further magnified, in comparison to the brightness variation pattern, and clearly display expressions of linear frontal features, meanders, and eddies with widths ranging from 1 to 10 km. The contrasts reaching up to $\pm 20\%$ are “statistically uniform” over the observed area, except in local areas adjacent to the clouds where the Sun glitter brightness is “contaminated” by the cloud shadows, and thus not applicable for the retrieval algorithm.

[10] The SAR NRCS contrasts shown in Figure 3b, $K_\sigma = (\sigma_0 - \bar{\sigma}_0) / \bar{\sigma}_0$, are defined using a similar moving average to obtain the variations of the NRCS relative to the mean backscatter $\bar{\sigma}_0$ with a spatial resolution of $30 \times 30 \text{ km}^2$. The qualitative comparison between the two contrast fields evidently reveals a significant relationship. Consistent with Johannessen *et al.* [2005], who suggested that the SAR expressions of the mesoscale features result from the short wave modulations by the surface current divergence field, the similarity between the MSS and NRCS features thus presumes that the MSS anomalies field also traces the surface current divergence field.

2.2. Physics of Similarity Between MSS and NRCS

[11] In order to further investigate and quantify the agreement between the MSS and SAR NRCS contrasts

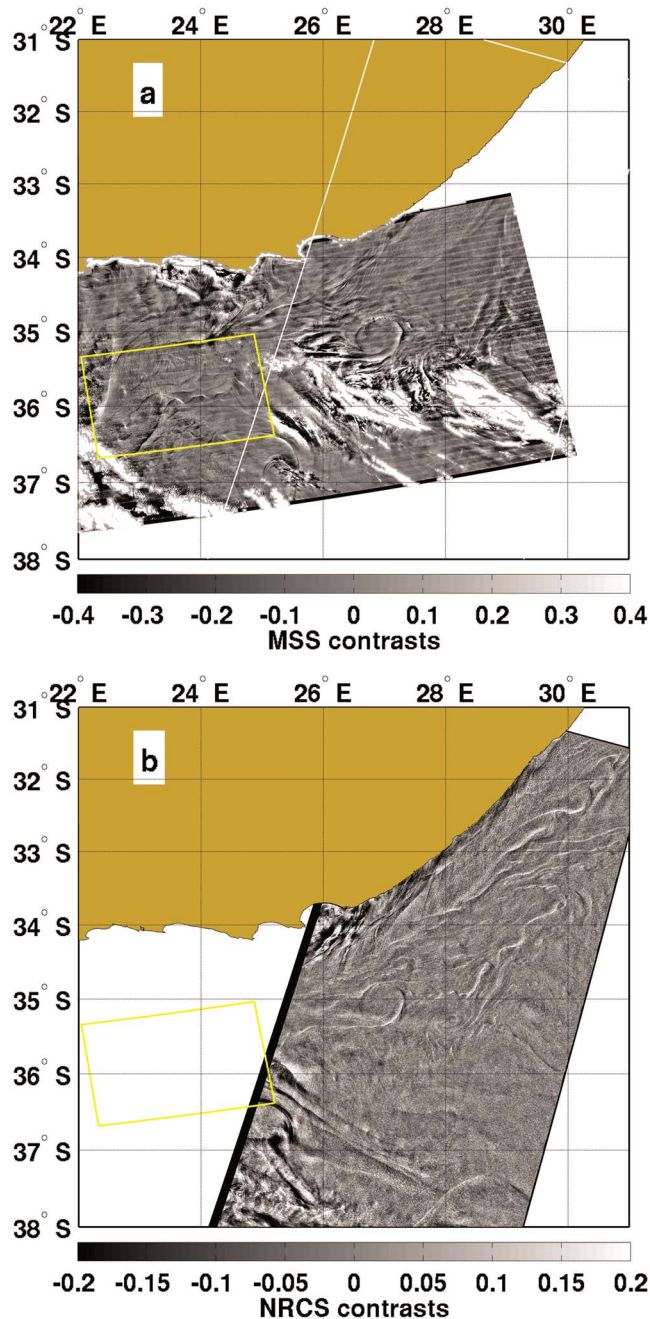


Figure 3. (a) The pattern of mean squared slope (MSS) contrasts derived from the Sun glitter brightness variations shown in Figure 2. (b) The near-coincident pattern of SAR normalized radar cross section (NRCS) contrasts. Yellow contour indicates position of the MSS image fragment shown in Figure 6a.

depicted in Figure 3, the radar imaging model (RIM) suggested by Kudryavtsev et al. [2005] and Johannessen et al. [2005] (hereinafter referred to as RIM-P1 and RIM-P2, correspondingly) is applied. As argued, the impact of the mesoscale ocean current on integral properties of the wind waves (like MSS and wave breaking parameters) is mainly

governed by divergence of the sea surface current field, $\nabla \cdot \mathbf{u}$.

[12] Hereinafter we derive the simplified equations relating the “surface roughness” signatures to the current features, which could further be used for quantitative analysis of SAR and optical images. The spectral transfer function, T (describing response of wind wave spectrum to wave-current interaction (see RIM-P1, equation (44)) reads

$$T = c_\tau \frac{\widehat{k}^{-3/2}}{1 + i \cdot c_\tau \widehat{k}^{-2} \widehat{K}} m_k(u_*/g) \nabla \cdot \mathbf{u}, \quad (1)$$

where the dimensionless relaxation time τ is estimated as $\tau = c_\tau (u_*/c)^{-2} \equiv c_\tau \widehat{k}$, u_* is the air friction velocity, c is the phase velocity, $\widehat{k} = ku_*^2/g$ is the dimensionless wave number of the wind waves, and $\widehat{K} = Ku_*^2/g$ is the wave number of the Fourier component of the surface current, with g being the gravity acceleration. Furthermore, $c_\tau = m_*/(2c_\beta)$ is a constant related to the wind wave growth rate parameter c_β (defined as $c_\beta \approx 0.04$) while the wind exponent of the spectrum m_* , $m_k = d \ln N / d \ln k$ is the wave number exponent of the omnidirectional spectrum of the wave action (see RIM-P1, section 3.2, for more details). Notice that in equation (1) the directionality effect (dependence on angle between wind and current directions) is ignored. Also, following the discussion and arguments of RIM-P1 and RIM-P2, only the divergence term, among different combinations of components of the current velocity gradients tensor, is retained because the other terms vanish after integration over the wind wave directions.

[13] Following equation (1), the amplitude of the transfer function has a maximum at

$$k_m \approx c_\tau^{1/2} g^{1/2} u_*^{-1} K^{1/2}, \quad (2)$$

corresponding to the spectral domain where the response of the wind waves on the surface current of a certain spatial scale is strongest. For instance, a transverse scale of the surface current of the order from 1 to 10 km will correspond to the maximum response within the wavelength domain ranging from 1 to 6 m. Hereinafter these waves are referred as the intermediate-scale gravity waves.

[14] The transfer function defined by equation (1) enables quantitative interpretation of the observed spatial variations of the MSS and NRCS. For this purpose, we define the wind wave saturation spectrum as $B \propto u_*^3/c$ [Phillips, 1985]. Then the MSS is

$$s^2 = \int_{k_c}^{k_p} B d \ln k \propto 2u_*^3/c_c,$$

where k_p and k_c are the wave numbers of the spectral peak and the spectral cutoff of shortest waves, respectively, and $c_c = c(k_c)$. The expression for the amplitude of the MSS variations

$$\bar{s}^2 = \int_{k_c}^{k_p} |T| B d \ln k$$

with the use of equation (1) is then approximately equal to

$$\tilde{s}^2 \propto m_k c_\tau^{1/2} (gK)^{-1/2} \nabla \cdot \mathbf{u}. \quad (3)$$

Thus the expression for the MSS contrasts reads

$$\tilde{s}^2/s^2 \propto m_k c_\tau^{1/2} u_*^{-1} (k_c K)^{-1/2} \nabla \cdot \mathbf{u} \quad (4)$$

and demonstrates that the MSS contrasts also get larger when the wind speed reduces. It also follows that the MSS contrasts are proportional to the magnitude of the current velocity drop over divergence zone and inversely proportional to the square root of its transverse scale.

[15] Notice that equation (4) describes the MSS variations caused by the direct interaction of intermediate-scale waves with the surface current (resulting from the action of the straining mechanism). Due to the relatively short relaxation time, the shorter wind waves do not “directly feel” the mesoscale current (since equation (1) approaches zero at large \hat{k}). However, as suggested in RIM, the mechanical disturbances of the sea surface by wave breaking serve as an additional energy input (along with wind forcing) to shorter wind waves. Therefore modulation of the small-scale roughness can be caused by the enhancement/suppression of breaking of the intermediate-scale waves on the mesoscale currents. This mechanism provides additional contribution (proportional to wave breaking modulations) to the MSS anomalies expressed by equation (4).

[16] Let us now consider response of the NRCS of the sea surface in the presence of mesoscale currents. As discussed by Kudryavtsev *et al.* [2003, 2005] and further analyzed recently by Mouche *et al.* [2007] and Guérin *et al.* [2010], the NRCS of the sea surface, σ_0^p , can be represented as the sum of a polarized composite Bragg-scattering term, σ_{br}^p , and a scalar contribution, σ_{wb} , associated with the longer waves or steeper singular events, which both depend on the fraction of the sea surface covered by breaking waves, q , i.e., $\sigma_{wb} = \sigma_{0wb}q$, where σ_{0wb} is a NRCS of the breaking zone. Using this decomposition, the NRCS of the sea surface reads

$$\sigma_0^p = \sigma_{br}^p + \sigma_{0wb}q. \quad (5)$$

[17] Although the Bragg scattering dominates the NRCS variations, the effect of the wave breaking is also important, especially at large incidence angles and HH polarization (see, e.g., RIM-P1, Figure 3). The term σ_{br}^p is proportional to the wave saturation spectrum B at the Bragg wave number \mathbf{k}_{br} : $\sigma_{br}^p = \pi G_p^2 \sin^{-4} \theta B(\mathbf{k}_{br})$, where G_p^2 is the geometric scattering coefficient. The Bragg waves are characterized by small spatial relaxation scale (of order 1 m) as compared with the surface current scales, and thus they do not interact directly with the mesoscale surface current (i.e., equation (1) in this range vanishes). However, as argued by RIM-P1, the mechanical disturbances of the surface by the breaking waves serve as an additional (to the wind input) energy source for shorter waves, and therefore we represent the wave spectrum as a sum: $B = B_0 + \Delta B_{wb}$, where B_0 is a wind forced part and ΔB_{wb} is a contribution of mechanical disturbances of the sea surface by breaking waves to the short wave spectrum. The latter term is proportional to the intensity of wave breaking events characterized here by the

fraction of the sea surface q : i.e., $\Delta B_{wb} \propto q$. Partial contribution of the surface disturbances by wave breaking to full wave spectrum, $p_{wb} = \Delta B_{wb}/B$, is strongly dependent on wave direction: at upwind directions p_{wb} is of order 0.1, but at crosswind directions (where wind forcing vanishes) its value attains $p_{wb} = 1$ (see, e.g., RIM-P1, Figure 1). Thus modulation of wave breaking on a mesoscale current may affect the NRCS via (1) their direct impact on radar backscatter (term $\sigma_{0wb}q$ in equation (5)) and (2) mechanical generation of short surface waves providing the Bragg scattering (term σ_{br}^p in equation (5)).

[18] Thus, following model (5), spatial variations of the NRCS, $\tilde{\sigma}_0^p$, caused by modulations of the wave breaking, \tilde{q} , are defined as

$$\tilde{\sigma}_0^p/\sigma_0^p = [(1 - P_{wb}^p)p_{wb} + P_{wb}^p]\tilde{q}/q, \quad (6)$$

where $P_{wb}^p(\varphi, \theta) = \sigma_{wb}/\sigma_0^p$ is partial contribution of wave breaking to the total NRCS, which is dependent on incidence angle, θ , and radar look direction, φ . As follows from (6), the field of the NRCS contrasts is similar to the field of wave breaking anomalies. However, the magnitude of the transfer coefficient (terms in the square bracket) depends on radar look direction relative to the wind vector. At crosswind radar look direction (where we recall that $p_{wb} = 1$) the NRCS contrasts follow the wave breaking contrasts, while at upwind directions the NRCS contrasts are weaker (with reduction factor depending on incidence angle and polarization).

[19] An analysis similar to MSS can be done for the estimation of the response of the wave breaking to the mesoscale currents (see RIM-P1, section 3.4, for more details). The fraction of the sea surface covered by breaking waves is defined through the length of the breaking wavefronts $\Lambda(k)$ as $q \propto \int \Lambda(k) dk$. Assuming that the wave breaking dissipation is proportional to the wind energy input, the quantity q can be expressed as

$$q \propto \int_{k_b}^{k_p} \beta B d \ln k \propto (u_* / c_b)^3,$$

where β is the wind wave growth rate, k_b is the wave number of the shortest breaking waves, and $c_b = c(k_b)$. The length of the breaking fronts is a strong nonlinear function of the saturation spectrum. For the adopted $B \propto u_*/c$, the quantity $\Lambda(k)$ is a cubic function of B . Therefore, the spatial variations of q in the presence of the mesoscale currents is defined as

$$\tilde{q} \propto 3 \int_{k_b}^{k_p} T \beta B d \ln k,$$

and with the use of equation (1) it can be expressed as

$$\tilde{q} \propto c_\tau m_k \ln(k_b/k_m) \frac{u_*}{g} \nabla \cdot \mathbf{u}. \quad (7)$$

[20] Modulation of the fraction of the sea surface covered by breaking waves is provided by the breaking in the “short wave” interval $c_\tau^{1/2} u_* K/g^{1/2} \equiv k_m < k < k_b$, i.e., in the interval from the shortest breaking waves (with $k = k_b$) to the waves

possessing maximal response to the impact of the current defined by equation (2). The expression for the wind wave breaking contrasts then reads

$$\frac{\tilde{q}}{q} \propto c_{\tau} m_k \ln(k_b/k_m) \frac{g}{u_{*k}^2} \omega_b^{-1} \nabla \cdot \mathbf{u}. \quad (8)$$

[21] As well as the MSS contrasts, the wave breaking variations follow the surface current divergence field. Since $m_k < 0$, the enhancement of the wave breaking (as well as the MSS contrasts) takes place in the zones of surface current convergence, where $\nabla \cdot \mathbf{u} < 0$. However, contrary to the MSS contrasts, the wave breaking contrasts decrease faster with increasing wind.

[22] Referring to equation (6) (with equation (8)) and equation (4), we thus conclude that both the expressions of the NRCS and the MSS contrasts trace the surface current divergence field, so that positive/negative contrasts correspond to convergence/divergence of the surface currents. However, we notice that the most favorable conditions for SAR imagery of the surface mesoscale currents take place when radar look direction is collinear with the crosswind direction.

[23] It is also important to emphasize that for optical spectrometers, the measurements are proportional to the sea surface slope probability density function (PDF). According to *Cox and Munk* [1954], the slope variances under low to moderate wind conditions (from 3 to 10 m/s) are relatively weak, with the standard deviation s of order $s \propto 0.1 - 0.2$. Away from the specular point at incidence angles of about $10^\circ - 20^\circ$, the PDF therefore rapidly drops and the slope variations become more dependent on the higher-order statistical moments, e.g., on the skewness and the kurtosis. Both these properties are associated with wave breaking, particularly small-scale breaking [*Chapron et al.*, 2000, 2002]. Therefore, in the area away from the specular point, the PDF shape and the Sun glitter brightness are strongly dependent on the fraction of the sea surface, q , covered by the steepest events. Correspondingly, the Sun glitter brightness features in such areas should also be determined by the wave breaking contrasts defined by equation (6).

[24] Thus both the Sun glitter features (independent on how far they are from the specular point) and the NRCS features can quantitatively trace the divergence of the mesoscale to submesoscale surface current field. Consequently, the sea surface signatures manifested in Figure 3 can certainly be considered as a tracer of the surface current divergence field.

3. Mesoscale Current Features Derived From SST and Their Relation to SAR and MSS Anomalies

[25] Comparing the sea roughness MSS and NRCS features (shown in Figure 3) with the SST patterns (shown in Figure 1), the very good qualitative agreement is striking. The main surface roughness changes coincide with local SST fronts. In general, this observation is not surprising, as ocean frontal areas are known for their intense cross-frontal dynamics and vertical motions (upwelling/downwelling). In this context, a model framework for the diagnostic calculations of the surface current field from the snapshot of the

SST field can be used to give additional experimental evidences for the relation of the sea surface roughness anomalies to the current divergence field.

3.1. Quasi-Geostrophic and Ageostrophic Circulations Reconstructed From the SST Field

[26] Advective influence of the Ekman transport and diabatic mixing in the Ekman layer can be considered as one of the main mechanisms generating the ageostrophic secondary circulation (ASC) in the vicinity of oceanic fronts [*Klein and Hua*, 1990; *Garrett and Loder*, 1981; *Thompson*, 2000; *Nagai et al.*, 2006]. Another mechanism was also recently discussed by *McWilliams et al.* [2009], analogous to self-induced frontogenesis to accelerate and sharpen temperature gradients from its related initial ageostrophic secondary circulation. Detailed consideration of all possible mechanisms is certainly beyond the scope of the present study. However, in order to interpret the coincident SST frontal features and the sea surface roughness anomalies, we restrict our analysis to the model framework based on the generation of the ASC by the Ekman forcing only. In so doing, we assume that the total oceanic current field can be represented as a sum of the quasi-geostrophic current (QGC), \mathbf{U} , the wind drift current \mathbf{u}^e (which can also include the inertial current), and the ASC field, \mathbf{u}^a , resulting from both the interaction of the Ekman flow with the QGC and the diabatic mixing in the Ekman layer. Thus the total current field is expressed as $\mathbf{u} = \mathbf{U} + \mathbf{u}^e + \mathbf{u}^a$.

[27] To the first order of the Rossby number the governing equations describing the dynamics of the ASC current field (see *Klein and Hua* [1990], *Garrett and Loder* [1981], *Thompson* [2000], and *Nagai et al.* [2006] for more details) reads

$$\begin{aligned} u_\beta^e \partial U_1 / \partial x_\beta - f u_2^a &= \nu_t \partial^2 U_1 / \partial x_3^2 \\ u_\beta^e \partial U_2 / \partial x_\beta + f u_1^a &= \nu_t \partial^2 U_2 / \partial x_3^2, \end{aligned} \quad (9)$$

where ν_t is the turbulent eddy viscosity assumed constant over the depth (inside the upper mixed Ekman layer), f is the Coriolis parameter, and $\beta = 1, 2$. In equation (9), the spatial scale of the wind field variability largely exceeds the cross-front spatial scale. Hence, taking into account the ‘‘thermal wind’’ balance equation, $\partial U_1 / \partial x_3 = (g/f) \partial \rho / \partial x_2$, $\partial U_2 / \partial x_3 = -(g/f) \partial \rho / \partial x_1$, and the equation for the ocean state $\rho = \rho_0(1 - \alpha T)$, the solution of equation (9) expressed in terms of the ASC reads

$$\begin{aligned} u_1^a &= -f^{-1} u_\beta^e \frac{\partial U_2}{\partial x_\beta} + (\nu_t g \alpha / f^2) \frac{\partial}{\partial x_3} \left(\frac{\partial T}{\partial x_1} \right), \\ u_2^a &= f^{-1} u_\beta^e \frac{\partial U_1}{\partial x_\beta} + (\nu_t g \alpha / f^2) \frac{\partial}{\partial x_3} \left(\frac{\partial T}{\partial x_2} \right), \end{aligned} \quad (10)$$

where g is the gravity acceleration and α is the thermal expansion coefficient. The first term in equation (10) describes the generation of the ASC due to the advective interaction of the Ekman flow with the QGC (the mechanism suggested by *Klein and Hua* [1990]), while the second term accounts for the generation of the ASC due to the frictional effect in the Ekman layer (the mechanism suggested by

Garrett and Loder [1981]). Both of these mechanisms would induce ocean current divergence in the vicinity of the thermal front as straightforwardly following from equation (10),

$$\nabla \cdot \mathbf{u} = -f^{-1} u_\beta^e \frac{\partial}{\partial x_\beta} \Omega + (\nu_t g \alpha / f^2) \frac{\partial}{\partial x_3} \Delta T, \quad (11)$$

where $\Omega_z = \partial U_2 / \partial x_1 - \partial U_1 / \partial x_2 \equiv \Delta \psi$ is the vorticity of the QGC, ψ is the stream function of the QG flow, and ΔT is the Laplacian of the water temperature. A balance of the left-hand side (LHS) of equation (11) with the first term in the RHS represents the solution obtained by Klein and Hua [1990] for the Ekman advective mechanism, while a balance with the second term in the RHS of equation (11) represents the solution suggested by Garrett and Loder [1981] for diabatic mixing mechanism of the ASC generation. Thus equation (11) can be considered as a generalized solution combining both mechanisms of the ASC generation due to the interaction of QGC with the Ekman layer.

[28] For simplicity, hereinafter the wind-driven currents are assumed to be the sum of classical Ekman current velocity $\mathbf{u}^{ek} = [\tau_2 / (fh), -\tau_1 / (fh)]$ and the inertial current $\mathbf{u}^i(t)$, i.e.,

$$\mathbf{u}^e = [\tau_2 / (fh), -\tau_1 / (fh)] + \mathbf{u}^i(t), \quad (12)$$

where $\boldsymbol{\tau} = v_*^2 [\cos \varphi_w, \sin \varphi_w]$, v_* is the friction velocity in the water, φ_w is the directions of the wind velocity vector, $h = (\nu_t / f)^{1/2}$ is the Ekman layer depth, and the inertial velocity $\mathbf{u}^i(t)$ can be prescribed following the time variability of the wind velocity. The turbulent eddy viscosity ν_t can be assessed following similarity between the marine and the atmospheric Ekman (planetary) boundary layers. For the stably stratified boundary layer the eddy viscosity is $\nu_t = \gamma \kappa v_* L$, where $\gamma \approx 0.2$ is a constant, $\kappa \approx 0.4$ is the Karman constant, and L is the Obukhov length scale [see, e.g., Brown, 1982]. By expressing L through the Brunt-Väisälä frequency for the upper ocean as $L = v_*^3 / (\kappa v_t N^2)$, the eddy viscosity reads

$$\nu_t = \gamma^{1/2} v_*^2 / N, \quad (13a)$$

and the Ekman layer depth can thus be expressed as

$$h = \gamma^{1/4} v_* / \sqrt{fN}. \quad (13b)$$

The estimates of h for, e.g., 10 m/s wind speed and $f = 10^{-4}$ are $h \approx 28$ m if the Prandtl ratio $N/f = 10$ and $h \approx 90$ m if $N/f = 1$.

[29] In order to define the sea surface current divergence (produced by ASC according to equation (11)), we need to introduce the QGC field. At mesoscales (10–500 km) and submesoscales (1–10 km), ocean dynamics is often that of a stably stratified rapidly rotating flow, with horizontal velocities, on average, much larger than vertical velocities. The motion is thus quasi two-dimensional and can be investigated in the frameworks of different approximations. Based on the surface quasi-geostrophic (SQG) dynamics [Held et al., 1995; Lapeyre and Klein, 2006], Isern-Fontanet et al. [2008] presented a practical approach for the reconstruction of the current velocity field at scales between 30 and 300 km from the snapshot of an SST image. Considering the SQG dynamics, the stream function of the QGC

$\hat{\psi}(\mathbf{k}, z)$ and the SST field $\hat{T}_s(\mathbf{k})$ in the Fourier space are linked by the following relation:

$$\hat{\psi}(\mathbf{k}, z) = \frac{g \alpha \hat{T}_s(\mathbf{k})}{f n_b k} \exp(n_0 k z), \quad (14)$$

where $n = N/f$ is the Prandtl ratio for the Brunt-Väisälä frequencies N_0 and N_b determining, respectively, the large-scale and mesoscale properties of the flow. Defining the QGC velocity through the stream function $\hat{\psi}$ as $\hat{\mathbf{U}} = (-ik_y \hat{\psi}, ik_x \hat{\psi})$ (or in physical space as $\mathbf{U} = (-\partial \psi / \partial x_2, \partial \psi / \partial x_1)$) we can then determine the ASC field through equation (10).

[30] In the Fourier space, the components of the ASC defined by equation (10) with equation (14), supplemented with estimations of the Ekman layer depth from equation (13b) and the eddy viscosity coefficient from equation (13a), are expressed through the SST as

$$\begin{aligned} (\hat{u}_1^a, \hat{u}_2^a) &= \frac{\alpha}{\gamma^{1/4} n_b^{1/2}} \cdot \frac{g v_*}{f^2} \left[s \cdot \sin(\varphi_w - \varphi) + i \gamma^{3/4} n_b^{1/2} \frac{v_* K}{|f|} \right] \\ &\cdot (K_1, K_2) \hat{T}_s, \end{aligned} \quad (15)$$

where $s = \text{sign}(f)$, i is the imaginary unit, φ is the direction of the wave number vector \mathbf{K} , and as before $\gamma = 0.2$. The second term in the bracket indicates the significance of the ratio of the mixing mechanism relative to the advective term. If we assume that $n_b = 10$ and $f = 10^{-4} \text{ s}^{-1}$, then this ratio is approximately equal 0.1 for a wind speed 10 m/s and $K = 2\pi/10^4 \text{ rad/m}$. In contrast, the ratio is approaching 1 for the shorter scale, e.g., $K = 2\pi/10^3 \text{ rad/m}$. The efficiency of this mixing mechanism increases both with a shortening of the QGC scales and an increasing wind speed. Hence, at low to moderate wind speeds and the current scale of order $K \propto 10^{-3} \text{ rad/m}$ or less, the Ekman transport mechanism (which in the general case includes also the inertial currents) dominates the ASC generation. From equation (15), the divergence of the surface current in the Fourier space

$\widehat{\nabla \cdot \mathbf{u}} = i K_\beta \hat{u}_\beta^a$ reads

$$\widehat{\nabla \cdot \mathbf{u}} = \frac{i \alpha}{\gamma^{1/4} n_b^{1/2}} \cdot \frac{g v_*}{f^2} \left[s \cdot \sin(\varphi_w - \varphi) + i \gamma^{3/4} n_b^{1/2} \frac{v_* K}{|f|} \right] K^2 \hat{T}_s. \quad (16)$$

Thus this equation directly links the divergence of the surface current to the SST field.

[31] The SST field available from the MODIS data (see Figure 1b) and the SAR wind field (see Figure 1a) are then used as input parameters to determine the surface current velocity field. In order to remove the large-scale SST variability, the spectral components with $K < 2\pi/100 \text{ rad/km}$ were filtered out. The spectral transform of the QG stream function was determined from equation (14), assuming $n_b = n_0 = 50$. As applied, the standard deviation of the derived surface QG velocities is then found equal to about 1 m/s. Use of these constants also helps to match the SAR derived surface velocity [Chapron et al., 2005; Johannessen et al., 2008] from the range Doppler measurements (not shown here). The background Ekman current, equations (12), (13a), and (13b), and ASC, equation (10), are calculated for the “mean observed” SAR southerly wind speed of 7 m/s.

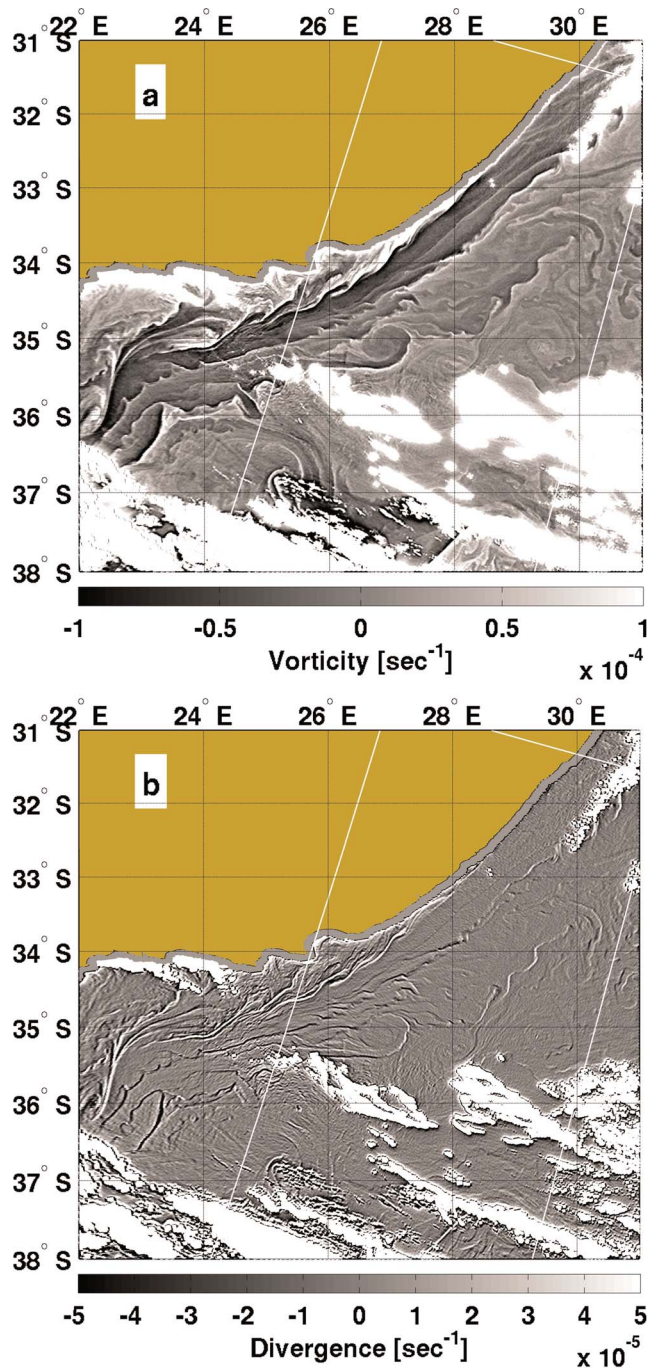


Figure 4. (a) The vorticity of the surface quasi-geostrophic current (QGC) derived from the SST shown in Figure 1b with the use of equation (14). (b) The surface current divergence field, $\nabla \cdot \mathbf{u}$, attributed to secondary ageostrophic circulation resulting from interaction of Ekman forcing (advective and mixing mechanisms) with QGC (see equations (11) and (16)). Note that the divergence field is inverted (i.e., field of $-\nabla \cdot \mathbf{u}$ is shown), and thus bright linear features correspond to the convergence zones and dark features correspond to the divergence zones.

[32] The vorticity of the QGC field and the surface current divergence derived from the observed SST field are shown in Figure 4. The QGC vorticity field exhibits a variety of mesoscale patterns and the existence of a “main jet” representing the Agulhas Current. In comparison to the surface current divergence, one reveals that the convergence/divergence patterns trace the gradients of the QGC vorticity field, which in turn is similar to the SST Laplacian field.

3.2. Relation of Reconstructed Divergence Field to SAR and MSS Anomalies

[33] Looking closer at the fragment of the SAR image shown in Figure 5a (it corresponds to the area above 36°S of the SAR image shown Figure 3) where the wind field was

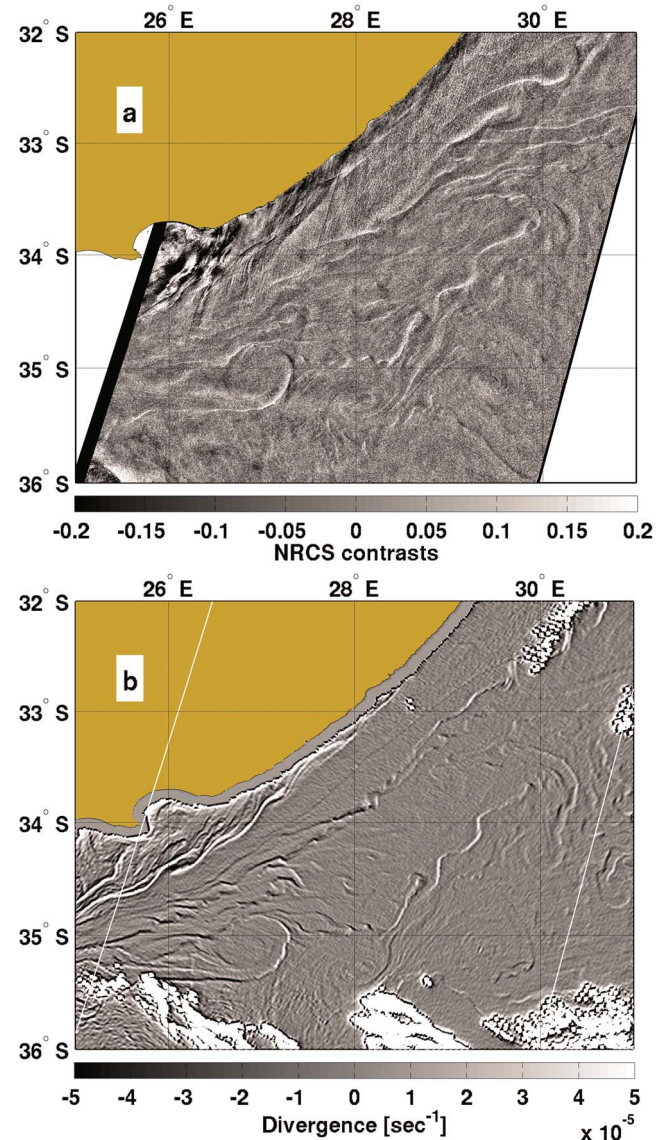


Figure 5. (a) A fragment of the SAR NRCS contrasts field shown in Figure 3 and (b) the corresponding fragment of the surface current divergence field shown in Figure 4. Bright areas in Figure 5b correspond to the current convergence, and dark areas correspond to the current divergence (see Figure 4 for more details).

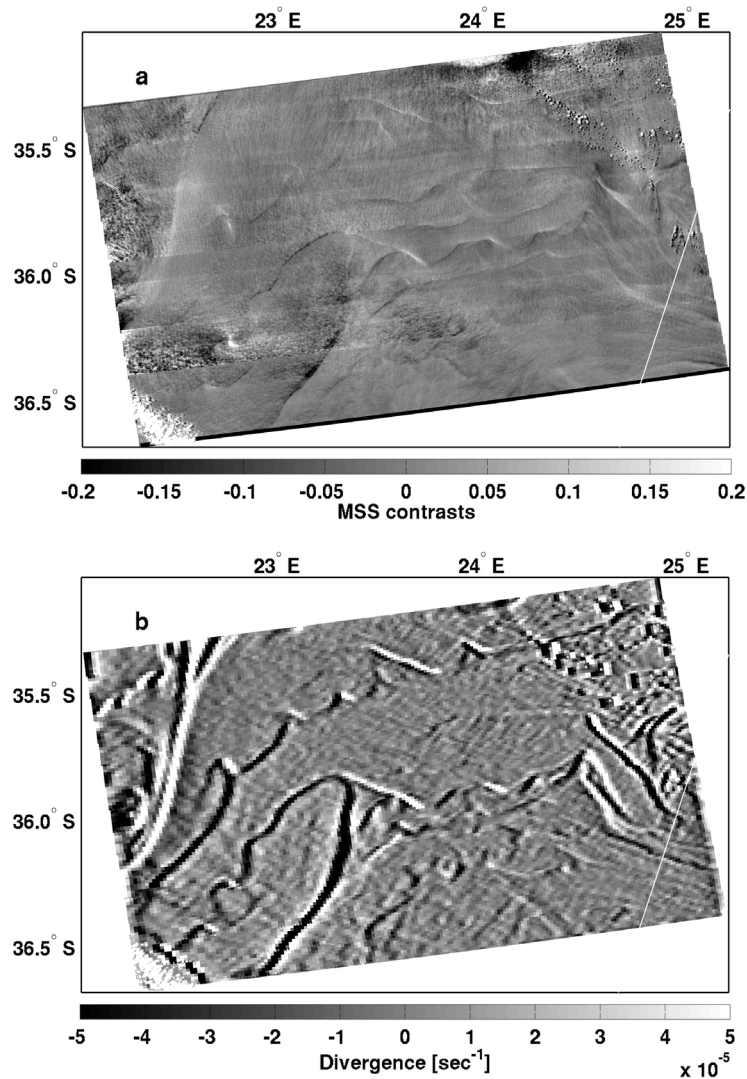


Figure 6. (a) Fragment of the MSS contrasts field, shown in Figure 3 (its position is indicated with yellow contour). (b) Field of the surface current divergence. The manifest difference between fields of surface current divergence shown in Figure 6b and in the corresponding area in Figure 4b is explained by the fact that $\nabla \cdot \mathbf{u}$ shown here was calculated for the local northerly wind, while $\nabla \cdot \mathbf{u}$ shown in Figure 4b in this area was calculated for the southerly wind (see text for more explanation). Bright areas correspond to the current convergence, and dark areas correspond to the current divergence (see Figure 4b for more details).

presumably uniform, the SAR image contrasts can be treated as surface manifestation of the oceanic mesoscale dynamics. The corresponding field of the surface current divergence is shown in Figure 5b.

[34] A visual inspection of Figure 5 shows that field of the NRCS contrasts and the divergence field (recall that there is a 5 h time interval between the SAR and MODIS acquisitions) have a very similar texture. Overall, the bright NRCS contrasts correspond to the current convergence while the dark contrasts represent the divergence zones. This observation, moreover, can be considered as experimental evidence of the model finding reported by RIM-P1 and RIM-P2 and simplified in equations (4), (8) with (6). On the other hand, if one believes that the relation between the NRCS anomalies and the current divergence exists, the apparent good agreement between SAR anomalies and the expected surface current divergence field would indicate that the

approach used for the reconstruction of the QGC and the ASC works properly and provides plausible estimations of the surface current field.

[35] A similar conclusion can be made with respect to the fragment of the MSS contrasts field shown in Figure 6a (enlarged fragment of the MSS field shown in Figure 3). The divergence field shown in Figure 6b was calculated for the local northerly wind. (Recall that the wind direction in this case is opposite to the one used before in calculations of the divergence field shown in Figure 4b). From equation (16) it follows that the wind direction affects the sign of $\nabla \cdot \mathbf{u}$, which explains the difference between Figure 6b and the corresponding fragment shown in Figure 4b. The choice of the wind direction in this case is suggested by the local wind direction as predicted by NCEP model (see Figure 1) and provides the “proper” sign of the divergence. Notice also that NCEP model predicts calm conditions over the observed

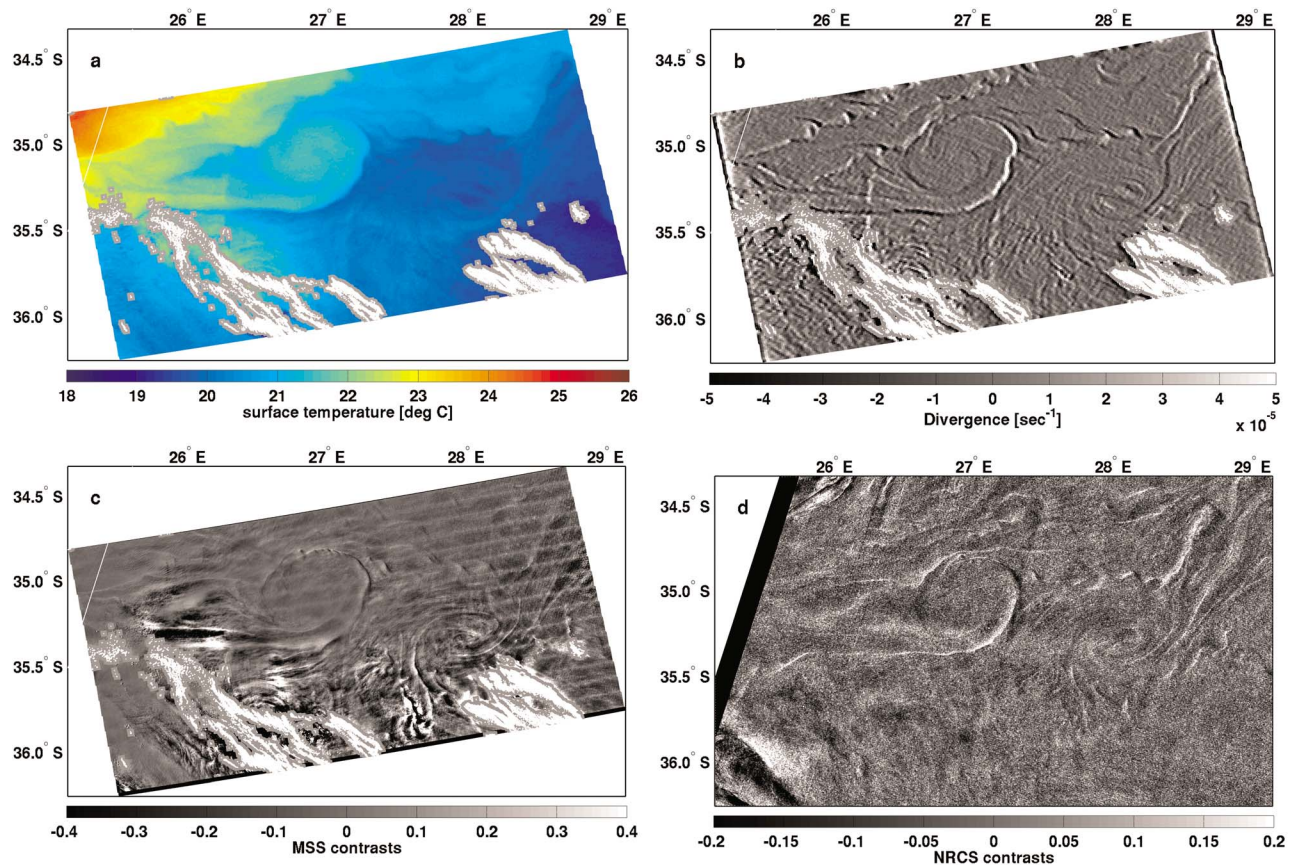


Figure 7. Multisensor expressions of a mushroom like eddy pair with a diameter of 120 km. (a) MODIS SST map and (b) surface current divergence field derived from the SST field. (c) The MSS contrasts derived from the MODIS and (d) the ASAR NRCS contrasts. The NRCS contrasts are in linear units. Bright areas in Figure 7b correspond to the current convergence, and dark areas correspond to the current divergence (see Figure 4b for more details).

area. However, local shape of the Sun glitter (see Figure 2a) indicates that the wind speed in this area is similar to other ones. Therefore in this calculation we use the same wind speed of 7 m/s as in the previous case. Careful inspection of the MSS and the divergence fields shows that, in general, the textural features in the two fields are quite similar, and the enhancement/suppression of the MSS follows in general the zones of the surface current convergence/divergence, similar to the SAR anomalies shown in Figure 5.

[36] In Figure 7 a mushroom-like eddy pair is distinctly visible in the SST field (see Figure 7a) and also clearly depicted in the surface current divergence field (Figure 7b). The corresponding MSS field (Figure 7c) and the SAR NRCS contrasts (Figure 7d) of the eddy acquired 5 h apart provide a striking demonstration of the strength in the synergetic approach. The textural agreement in the observed SST, NRCS, and MSS surface expressions together with the surface convergence map, in particular for the anticyclone eddy, provides clear evidence that the synergetic approach strengthens the quantitative analyses of the upper ocean dynamics.

3.3. RIM Simulations

[37] The sea surface current field (consisting of the sum of the QGC, the Ekman drift, and the ASC) derived from the MODIS SST and ENVISAT ASAR wind fields can further

be invoked into the Radar Imaging Model (RIM) for simulations of NRCS and MSS signatures as suggested by RIM-P1 and RIM-P2. The RIM simulates the manifestations of the surface current features, temperature fronts, and slicks in terms of modulations of the wind wave spectra, MSS, wave breaking, and the NRCS.

[38] The simulated surface manifestations of the mushroom-like eddy pair in terms of the MSS, the wave breaking, and the NRCS contrasts are shown in Figure 8 for an incidence angle of 30° and a radar look direction of 20° (in respect to the wind direction). As anticipated, the patterns of these 2-D fields are very similar to the structure of the surface current convergence. A careful inspection shows that the contrast enhancement of all three quantities takes place in the zones of current convergence (bright areas in Figure 8a), while suppression occurs in the divergence zones (dark areas). This result of numerical simulations corresponds to the simplified solutions defined by equation (4), equation (6), and equation (8). Recall that due to small relaxation scale (order of 1 m) Bragg waves are unable to interact with the mesoscale currents directly, via the “straining mechanism.” As argued by Kudryavtsev *et al.* [2005], manifestations of mesoscale surface current features in the NRCS originate from the action of wave breaking, which provides stronger/weaker mechanical disturbances

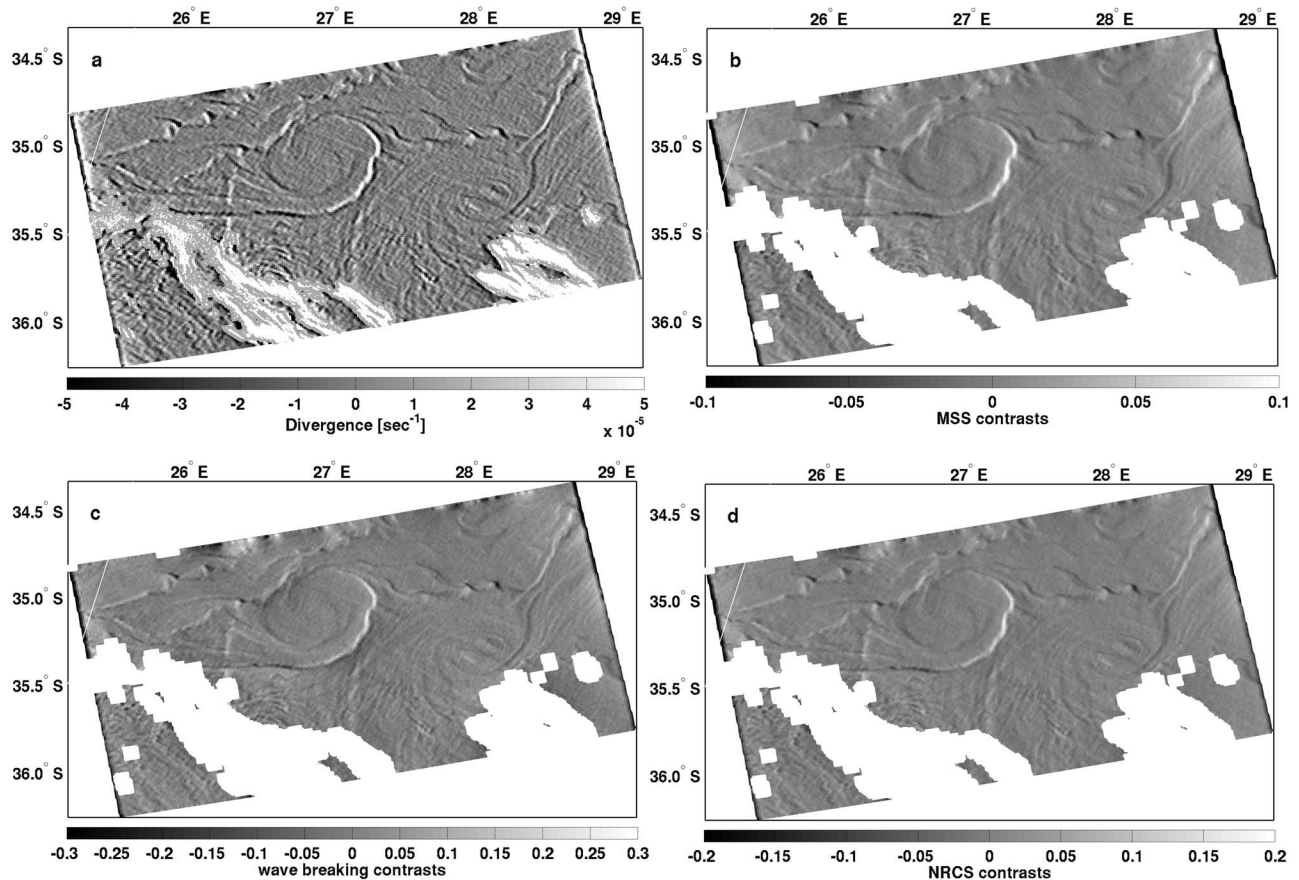


Figure 8. (a) Divergence of the surface current derived from the SST field (see Figure 7a). Bright/dark areas correspond to the current convergence/divergence. The remaining plots are RIM simulations of the surface manifestations of the mushroom-like eddy pair presented in the form of the contrasts in the (b) MSS, (c) wave breaking, and (d) NRCS.

of the surface in the convergent/divergent zones. These mechanical disturbances lead to the local enhancement/suppression of the Bragg waves and hence the modulation of the radar backscattering. Comparing the fields of simulated NRCS and MSS contrasts with the observations shown in Figure 7, one may notice that the magnitudes of the model contrasts are consistent with the observed values. Since RIM was extensively tested against available data (see RIM-P1), this fact presumes that the reconstructed field of the surface current divergence may be considered as close to the “real” field. It is worth noting that the simulations of the NRCS contrasts for the same eddy pair without accounting for the impact of wave breaking on both the NRCS and Bragg waves modulations (a “standard” relaxation model) gives NRCS contrasts 4 orders of magnitude less than that shown in Figure 8.

[39] Comparison of the numerical RIM simulations (shown in Figure 8) with the simplified relations expressed in equation (4) and equation (8) provides an opportunity to assess the proportionality constants for further use of the simplified solutions in practical applications. We arrived at

$$\begin{aligned} \frac{\tilde{s}^2}{s^2} &= -\frac{c_s}{u_* (k_c K)^{1/2}} \nabla \cdot \mathbf{u} \\ \frac{\tilde{q}}{q_0} &= -c_q \ln \left(\frac{u_* k_b}{g^{1/2} K^{1/2}} \right) \frac{g}{u_*^2 k_b} \omega_b^{-1} \nabla \cdot \mathbf{u} \end{aligned} \quad (17)$$

with $c_s = 180$ and $c_q = 470$ at $k_c = (g/\gamma)^{1/2}$ and $k_b = k_R/10$ (γ is the surface tension, k_R is radar wave number).

[40] All in all, the analysis of SAR and the MSS signatures of the subscale and mesoscale upper ocean dynamics show that they have a distinct textural similarity with the surface current divergence field, with contrasts of about the same magnitude, although slight differences in the details of the contrast patterns can be found. This is presumably resulting from (1) a shortcoming in the reconstruction of the surface current and the divergence field from the MODIS derived SST snapshot; (2) uncertainties in the local wind field, wind drift, Ekman current, and inertial currents estimates; and (3) temporal evolution of the mesoscale features in the near 5 h time interval between the ASAR and MODIS acquisitions. Nevertheless, the overall agreement is very promising and clearly demonstrates the feasibility of retrieving quantitative estimates of the upper layer dynamics from the multisensor surface expressions of mesoscale features.

4. Conclusion

[41] Hitherto the complete quantitative understanding of the SAR imaging of surface roughness modulations induced by the surface current divergence and convergence field has been insufficient. In this study a new synergetic approach for quantitative analysis of SAR and imaging

spectrometer data, including the infrared channels, has been presented and applied.

[42] Notably, this synergetic approach clearly demonstrates that the sea surface mean square slope (MSS) anomalies derived from the Sun glitter imagery (formed by full range of waves, from capillaries to energy containing waves) compare very well to SAR NRCS anomalies. Both fields are then found to spatially correspond to frontal areas presenting large SST gradients. Since typical frontal region could consist of an along-front jet with intense cross-frontal dynamics and vertical motion, such results were already expected following RIM-P1 and RIM-P2 results.

[43] Building on the assumption that the upper ocean circulation is quasi two-dimensional, the surface quasi-geostrophic current (QGC) field is reconstructed from snapshot of band-pass-filtered satellite infrared SST data, following the surface quasi-geostrophic (SQG) dynamics. As this resulting QGC field is nondivergent, its direct interaction with the wind waves results in weak surface manifestation of mesoscale current features, as already shown by RIM-P1 and RIM-P2. More likely, it is the possible interaction of the wind-driven upper layer motion with the QGC field (via Ekman advective and mixing mechanisms, as suggested by Klein and Hua [1990] and Garrett and Loder, 1981) that can result in the generation of a sufficiently strong ageostrophic surface current, producing large surface convergence and divergence. Under the proposed assumption, intense cross-frontal dynamics occur near sharp horizontal gradients of the vorticity of the QGC, as well as strong vertical gradients of the QGC velocity.

[44] Accordingly, one may consider the observed striking agreement and correspondence between roughness anomalies and SST gradients as “experimental evidence” of the fact that the impact of the surface current divergence on the short wind waves constitutes the governing mechanism leading to manifestation of mesoscale surface current features in the form of the “surface roughness” anomalies. On the other hand, the correlation between the surface roughness anomalies and the model surface current divergence strongly suggests that the model framework for the reconstruction of the mesoscale surface current is quite reliable.

[45] The surface current field derived from MODIS SST and SAR wind data was also used as the input parameters for the RIM forward simulations and clearly documents that the observed anomalies in the SAR NRCS, as well as anomalies of the MSS derived from the MODIS data, represent the surface expressions of the ocean current convergence/divergence areas along meandering fronts and eddies.

[46] In summary, the proposed synergetic approach combining SST, Sun glitter brightness, and SAR data, possibly augmented by other external sources of lower-resolution information (e.g., altimeter and scatterometer), provides consistent and quantitative determination of the location and intensity of the surface current convergence/divergence (upwelling/downwelling). This, in turn, establishes an important and promising step toward advances in the quantitative interpretation and understandings of the upper ocean dynamics from their 2-D satellite surface expressions.

[47] **Acknowledgments.** Core support for this study was provided by the joint CNES-EUMETSAT funded OSTST project Ocean3D and the ANR funded REDHOTS project. ENVISAT ASAR data were provided by ESA through the study contract 18709/05/I-LG. Support of Russian

Federation government grants 11.G34.31.0078 for the Russian State Hydro-meteorological University and the Federal Programme under contract N14.740.11.0201 are gratefully acknowledged.

References

- Alpers, W., and I. Hennings (1984), A theory of the imaging mechanism of underwater bottom topography by real and synthetic aperture radar, *J. Geophys. Res.*, *89*(C6), 10,529–10,546, doi:10.1029/JC089iC06p10529.
- Beal, R., V. Kudryavtsev, D. Thompson, S. Grodsky, D. Tilley, V. Dulov, and H. Graber (1997), The influence of the marine atmospheric boundary layer on ERS-1 synthetic aperture radar imagery of the Gulf Stream, *J. Geophys. Res.*, *102*(C3), 5799–5814, doi:10.1029/96JC03109.
- Brown, R. (1982), On two-layer models and the similarity functions for the PBL, *Boundary Layer Meteorol.*, *24*, 451–463, doi:10.1007/BF00120733.
- Chapron, B., V. Kerbaol, D. Vandemark, and T. Elfouhaily (2000), Importance of peakedness in sea surface slope measurements and applications, *J. Geophys. Res.*, *105*, 17,195–17,202, doi:10.1029/2000JC900079.
- Chapron B., D. Vandemark, and T. Elfouhaily (2002), On the skewness of the sea slope probability distribution, in *Gas Transfer at Water Surfaces*, *Geophys. Monogr. Ser.*, vol. 127, edited by M. A. Donelan et al., pp. 59–63, AGU, Washington, D. C.
- Chapron, B., F. Collard, and F. Ardhum (2005), Direct measurements of ocean surface velocity from space: Interpretation and validation, *J. Geophys. Res.*, *110*, C07008, doi:10.1029/2004JC002809.
- Cox, C., and W. Munk (1954), Measurement of the roughness of the sea surface from photographs of the Sun's glitter, *J. Opt. Soc. Am.*, *44*, 838–850, doi:10.1364/JOSA.44.000838.
- Espedal, H. A., O. M. Johannessen, J. A. Johannessen, E. Dano, D. R. Lyzenga, and J. C. Knulst (1998), COASTWATCH'95: ERS 1/2 SAR detection of natural film on the ocean surface, *J. Geophys. Res.*, *103*(C11), 24,969–24,982, doi:10.1029/98JC01660.
- Gade, M., W. Alpers, H. Huehnerfuss, H. Masuko, and T. Kobayashi (1998), Imaging of biogenic and anthropogenic ocean surface films by the multifrequency/multipolarization SIR-C/X-SAR, *J. Geophys. Res.*, *103*(C9), 18,851–18,866, doi:10.1029/97JC01915.
- Garrett, C. J. R., and J. W. Loder (1981), Dynamical aspects of shallow sea fronts, *Philos. Trans. R. Soc. London A*, *302*, 563–581, doi:10.1098/rsta.1981.0183.
- Gasparovic, R. F., J. A. Apel, and E. S. Kasichke (1988), An overview of the SAR internal wave signature experiment, *J. Geophys. Res.*, *93*(C10), 12,304–12,316, doi:10.1029/JC093iC10p12304.
- Guérin, C.-A., G. Sorian, and B. Chapron (2010), The weighted curvature approximation in scattering from sea surfaces, *Waves Random Complex Media*, *20*(3), 364–384, doi:10.1080/17455030903563824.
- Held, I. M., R. T. Pierrehumbert, S. T. Garner, and K. L. Swanson (1995), Surface quasi-geostrophic dynamics, *J. Fluid Mech.*, *282*, 1–20, doi:10.1017/S0022112095000012.
- Hennings, I., J. Matthews, and M. Metzner (1994), Sun glitter radiance and radar cross-section modulations of the sea bed, *J. Geophys. Res.*, *99*(C8), 16,303–16,326, doi:10.1029/93JC02777.
- Hu, C., X. Li, W. G. Pichel, and F. E. Muller-Karger (2009), Detection of natural oil slicks in the NW Gulf of Mexico using MODIS imagery, *Geophys. Res. Lett.*, *36*, L01604, doi:10.1029/2008GL036119.
- Isern-Fontanet, J., G. Lapeyre, P. Klein, B. Chapron, and M. W. Hecht (2008), Three-dimensional reconstruction of oceanic mesoscale currents from surface information, *J. Geophys. Res.*, *113*, C09005, doi:10.1029/2007JC004692.
- Jackson, C. (2007), Internal wave detection using the Moderate Resolution Imaging Spectroradiometer (MODIS), *J. Geophys. Res.*, *112*, C11012, doi:10.1029/2007JC004220.
- Jansen, R., C. Shen, S. Chubb, A. Cooper, and T. Evans (1998), Subsurface, surface, and radar modeling of a Gulf Stream current convergence, *J. Geophys. Res.*, *103*(C9), 18,723–18,743, doi:10.1029/98JC01195.
- Johannessen, J. A., R. Shuchman, G. Digranes, D. Lyzenga, W. Wackerman, O. Johannessen, and P. Vachon (1996), Coastal ocean fronts and eddies imaged with ERS-1 synthetic aperture radar, *J. Geophys. Res.*, *101*, 6651–6667, doi:10.1029/95JC02962.
- Johannessen, J. A., V. Kudryavtsev, D. Akimov, T. Eldevik, N. Winther, and B. Chapron (2005), On radar imaging of current features: 2. Mesoscale eddy and current front detection, *J. Geophys. Res.*, *110*, C07017, doi:10.1029/2004JC002802.
- Johannessen, J. A., B. Chapron, F. Collard, V. Kudryavtsev, A. Mouche, D. Akimov, and K.-F. Dagestad (2008), Direct ocean surface velocity measurements from space: Improved quantitative interpretation of Envisat ASAR observations, *Geophys. Res. Lett.*, *35*, L22608, doi:10.1029/2008GL035709.
- Klein, P., and B. Hua (1990), The mesoscale variability of the sea surface temperature: An analytical and numerical model, *J. Mar. Res.*, *48*, 729–763.

- Kudryavtsev, V., D. Hauser, G. Caudal, and B. Chapron, (2003), A semi-empirical model of the normalized radar cross-section of the sea surface: 1. Background model, *J. Geophys. Res.*, *108*(C3), 8054, doi:10.1029/2001JC001003.
- Kudryavtsev, V., D. Akimov, J. A. Johannessen, and B. Chapron (2005), On radar imaging of current features: 1. Model and comparison with observations, *J. Geophys. Res.*, *110*, C07016, doi:10.1029/2004JC002505.
- Kudryavtsev, V., A. Myasoedov, B. Chapron, J. Johannessen, and F. Collard (2012), Joint sun-glitter and radar imagery of surface slicks, *Remote Sens. Environ.*, in press.
- Lapeyre, G., and P. Klein (2006), Dynamics of the upper oceanic layers in terms of surface quasigeostrophy theory, *J. Phys. Oceanogr.*, *36*, 165–176, doi:10.1175/JPO2840.1.
- Lin, I.-I., L.-S. Wen, K.-K. Liu, W.-T. Tsai, and A. K. Liu (2002), Evidence and quantification of the correlation between radar backscatter and ocean colour supported by simultaneously acquired in situ sea truth, *Geophys. Res. Lett.*, *29*(10), 1464, doi:10.1029/2001GL014039.
- Lyzenga, D. R., and J. R. Bennett (1988), Full-spectrum modeling of synthetic aperture radar internal wave signature, *J. Geophys. Res.*, *93*(C10), 12,345–12,354, doi:10.1029/JC093iC10p12345.
- Marmorino, G. O., R. W. Jansen, G. R. Valenzuela, C. L. Trump, J. S. Lee, and J. A. C. Kaiser (1994), Gulf Stream surface convergence imaged by synthetic aperture radar, *J. Geophys. Res.*, *99*, 18,315–18,328, doi:10.1029/94JC01643.
- McWilliams, J. C., F. Colas, and M. J. Molemaker (2009), Cold filamentary intensification and oceanic surface convergence lines, *Geophys. Res. Lett.*, *36*, L18602, doi:10.1029/2009GL039402.
- Mouche, A. A., B. Chapron, N. Reul, D. Hauser, and Y. Quilfen (2007), Importance of the sea surface curvature to interpret the normalized radar cross section, *J. Geophys. Res.*, *112*, C10002, doi:10.1029/2006JC004010.
- Munk, W., L. Armi, K. Fischer, and F. Zachariassen (2000), Spirals on the sea, *Proc. R. Soc. A*, *456*, 1217–1280.
- Nagai, T., A. Tandon, and D. L. Rudnick (2006), Two-dimensional ageostrophic secondary circulation at ocean fronts due to vertical mixing and large-scale deformation, *J. Geophys. Res.*, *111*, C09038, doi:10.1029/2005JC002964.
- Phillips, O. M. (1985), Spectral and statistical properties of the equilibrium range in wind-generated gravity waves, *J. Fluid Mech.*, *156*, 505–531, doi:10.1017/S0022112085002221.
- Romeiser, R., and W. Alpers (1997), An improved composite surface model for the radar backscattering cross section of the ocean surface: 2. Model response to surface roughness variations and the radar imaging of under-water bottom topography, *J. Geophys. Res.*, *102*(C11), 25,251–25,267, doi:10.1029/97JC00191.
- Stoffelen, A., and D. Anderson (1997), Scatterometer data interpretation: Estimation and validation of the transfer function CMOD4, *J. Geophys. Res.*, *102*(C3), 5767–5780, doi:10.1029/96JC02860.
- Thompson, L. (2000), Ekman layers and two-dimensional frontogenesis in the upper ocean, *J. Geophys. Res.*, *105*, 6437–6451, doi:10.1029/1999JC900336.
- B. Chapron, Institut Français de Recherche pour l'Exploitation de la Mer, F-29280 Plouzané, France.
- F. Collard, Direction of Radar Applications, CLS, 115, rue Claude Chappe, F-29280 Plouzané, France.
- J. A. Johannessen, Nansen Environmental and Remote Sensing Center, Thormøhlensgate 47, Bergen N-5006, Norway.
- V. Kudryavtsev and A. Myasoedov, Nansen International Environmental and Remote Sensing Center, 7, 14th Line, Office 49, St. Petersburg 199034, Russia.